ORIGINAL RESEARCH ARTICLE

Gold (Au)-Doped Lead Sulfide-Polyvinyl Alcohol (PbS-PVA) Nanocomposites for High-Performance, Flexible Memristors

Surbhi Pathania[1] · Jehova Jire L. Hmar[2] · Vinay Kumar[1] · Onkar Nath Verma[1] · Tanuj Kumar[3] ·
Chinnamuthu Paulsamy[4]

Abstract

This study demonstrates flexible non-volatile resistive switching memory using gold (Au)-doped PbS-PVA nanocomposites deposited on patterned ITO-coated flexible PET substrate. X-ray photoelectron spectroscopy study showed the presence of oxidation states of lead (Pb), sulphur (S) and gold (Au) ions in the nanocomposites. The fabricated Al/Au-PbS-PVA/ITO-coated flexible PET substrate device showed a bistable non-volatile flexible memristor and revealed superior behaviour in the current ratio (I_{ON}/I_{OFF}) of ON-state and OFF-state compared to the control device Al/PbS-PVA/ITO-coated flexible PET substrate due to the presence of Au nanoparticles in PbS-PVA composites. The incorporation of Au nanoparticles in PbS-PVA nanocomposite increases charge carrier injection that further enhances the current ratio (I_{ON}/I_{OFF}) between the ON- and OFF-states of the device up to 10^6 with lower operating voltage at $\pm$ 2V. The reversible resistance switching between OFF-state and ON-state was repeated for 100 cycles, and the two resistance states showed endurance and stability. Even after the applied bias was removed, the device maintained its OFF- and ON-states, showing bistable non-volatile memory. The fabricated flexible memristor was measured for retention, stability and flexibility by constantly bending the device from 70° bending angle to 120° bending angle and without bending (180°). Interestingly, I-V characteristics after bending the device from 180° to 70° remained stable and unvariable. Therefore, the fabricated flexible memristor holds robust potential to be used in advanced flexible electronic applications.

✉ Jehova Jire L. Hmar
   jehovajire52@gmail.com

1 Department of Physics and Astronomical Sciences,
   Central University of Jammu, Rahya-Suchani, Samba,
   Jammu and Kashmir 181143, India

2 Department of Physics, Netaji Subhas University
   of Technology (NSUT), Sector-3, Dwarka,
   New Delhi 110078, India

3 Department of Nanoscience and Materials, Central
   University of Jammu, Rahya-Suchani, Samba,
   Jammu and Kashmir 181143, India

4 Department of ECE, NIT, Chümoukedima,
   Nagaland 797103, India

Graphical Abstract
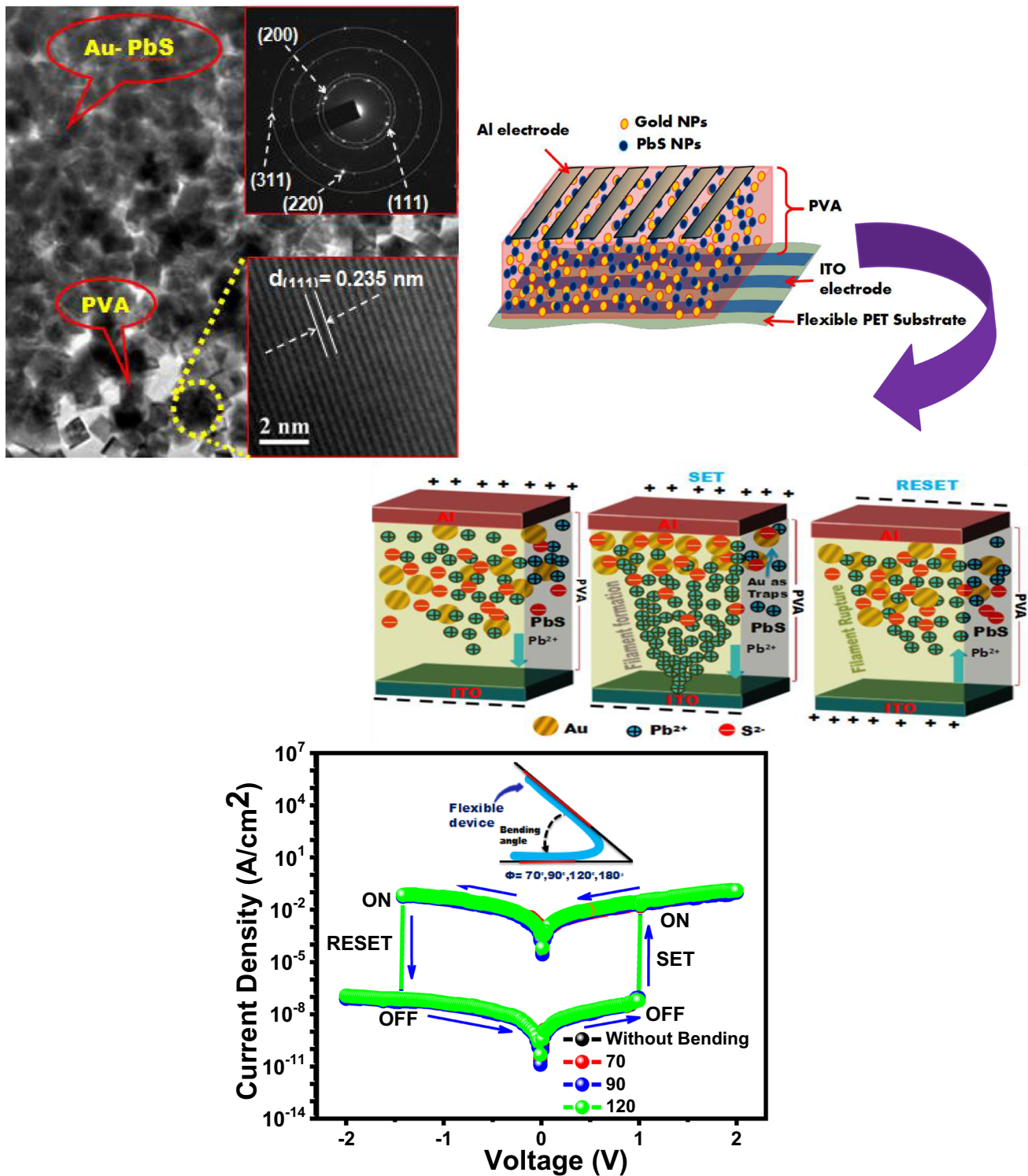
Introduction

Resistive random access memory (RRAM) is an appropriate candidate for next-generation memory devices. RRAM devices possess advantages of low operation voltage, large storage density and less power consumption. Resistive switching behaviour is observed in memory devices which tends to change resistance when an appropriate voltage is applied across the electrodes. To improve the device performance, it is important to identify the exact physical transport mechanism and how it relates to resistive switching phenomena. The most commonly noticed conduction mechanisms are Poole-Frenkel emission, Schottky emission, space-charge-limited conduction (SCLC), trap-assisted tunnelling and hopping conduction. Resistive switching layers have been so far developed in inorganic, organic and hybrid materials.[1]. Hybrid nanocomposite materials comprising inorganic semiconducting in an organic matrix are an emerging class of new materials that can be used in a variety of applications including sensors,[2] displays,[3] photovoltaics,[4] photonic devices,[5] non-volatile memory devices[6] and neuromorphic computing systems.[7,8] Boybat et al.[9] demonstrated a work based on phase change memory devices, providing a significant step towards the realization of large-scale energy efficient neuromorphic computing systems. Using these memristive devices, synaptic efficacy can be realized using Ohm's law, inducing two essential synaptic attributes, namely potentiation and depression. An increase and decrease in the synaptic weight is referred to as potentiation and depression, respectively. Lead sulphide (PbS) is an essential semiconductor material with many eminent optical and electrical properties and it has been extensively applied in nonlinear optical devices, IR detectors and display devices.[10] PbS is binary IV-VI semiconductor material with a narrow band gap ~ 0.41 eV at room temperature, and a large exciton Bohr radius (~18 nm). PbS is direct band gap semiconductor material, and self-assembled PbS quantum dots (QDs) are fabricated at low temperature to ensure the uniform distribution of QDs in the resistive switching memory devices.[11] The advantages of growing hybrid semiconductor nanostructures inside an insulating polymer matrix include the prevention of oxidation and coalescence of the nanostructures, as well as acting as an outstanding capping agent for the memory device.[12] Hmar et al. performed the flexible studies of high dielectric based on Al/PbS-PVA/flexible ITO coated on PET substrate devices at different bending angles.[10] Sarma et al. demonstrated the synthesis of PbS QDs embedded in polyvinyl alcohol (PVA) matrix for memory application.[13] Chen et al. demonstrated development of advanced high-density data storage technology utilizing PbS QDs in conducting polymer poly(methyl methacrylate) (PMMA) matrix.[14] Various reports suggest that metal nanoparticles on the surface of semiconductors can boost the charge separation and polarization with an increase in charge carrier in the hybrid semiconductor nanostructures.[15] Metal nanoparticles may also result in enhancing the localized

electric field in the memory device.[16] The incorporation of metallic nanoparticles such as Ag, Au, Mo, Co, and Cu in semiconductor nanostructures contribute to charge-trapping and can effectively improve the resistive switching memory.[17] Gold nanoparticles have been noted for their optical resonance in the visible range as well as the local field enhancement of light interaction with the resonant system.[18] The photonic properties of gold are appealing for materials applications, biochemical and biomedical usage.[19] Au nanoparticles exhibit the remarkable potential of enhancing the electrical performance of a memory device by either trapping electrons or holes.[20]

In this paper, we synthesize Au nanoparticles doped in PbS-PVA nanocomposites and deposited Au-doped PbS-PVA nanocomposites on ITO-coated flexible PET substrate. We also study the flexible non-volatile resistive switching memory device based on Au-doped PbS-PVA nanocomposites deposited on ITO-coated flexible PET substrate. PbS demonstrates strong quantum confinement effects attributed to the small effective masses of its electrons and holes and its high dielectric constant. PVA has excellent properties such as isolating dielectric and supporting film for transportation of charge carriers and preventing leakage of current. The incorporation of Au nanoparticles in PbS-PVA composite enhances the ON-OFF current ratio of a device up to 10^6 with low voltage at ±2V. The charge transport mechanism of the fabricated device is possibly contributed to by both trapping and detrapping of SCLC and the formation and rupture of filaments. This non-volatile memory device exhibits bipolar resistive switching behaviour and is a promising candidate for flexible resistive non-volatile memory. Attractively, the fabricated Al/Au-PbS-PVA/ITO-coated flexible PET substrate demonstrates non-volatile bistable resistive random access memory (RRAM). Because the fabricated memory device possesses retention, stability and flexibility properties, it has the potential to be used in advanced flexible non-volatile RRAM memory application.

Experimental Details

Preparation of Gold Nanoparticles

Gold nanoparticles (Au NPs) were prepared using Frens method.[21] In this method, 50 ml aqueous solution of chloroauric acid (HAuCl$_4$) was heated at boiling temperature. After that, 0.8 ml of trisodium citrate solution was added to the previous solution with continuous stirring and the boiling temperature is constantly maintained. The boiling solution was blue in colour that changed to reddish pink, indicating the formation of Au NPs.

Preparation of Au/PbS-PVA Nanocomposites

Au/PbS-PVA nanocomposites were prepared using chemical bath deposition (CBD).[22] A transparent polyvinyl alcohol (PVA) solution was made by dissolving 4 g of solid PVA $(C_2H_4O)_n$ (where $n = 1700$) in 150 ml DI water, then heating and stirring for 2 h at 95°C. When the temperature dropped to 40°C, an aqueous solution was added to the previous solution, containing 4.98 mmol lead acetate (99%, Nice) and 0.02 mol NaOH (97%, Merck). After a few minutes, 11.82 mmol of CH_4N_2S (thiourea) was added to the solution. The Au/PbS-PVA nanocomposites were prepared when Au solution was added to the solution of PbS-PVA in 1:10 [Au: PbS-PVA] concentration ratio. Both the PbS/PVA films and Au/PbS-PVA films were deposited on the flexible ITO-coated polyethylene terephthalate (PET) substrates by dipping for 30 min into the PbS/PVA composite solution and Au/PbS-PVA composite solution at 80°C bath temperature, respectively. The prepared thin films were dried in air for a few hours and kept for further use.

Device Fabrication

For the bottom electrode (BE), ITO-coated flexible PET substrate was used. Au-PbS/PVA nanocomposites were deposited on patterned ITO-coated flexible PET substrate using chemical bath deposition (CBD). The samples were left to dry in open air. Then, aluminium metal was deposited as the top electrode (TE) using thermal evaporation through a shadow mask with an active area of 2×10^{-6} m^2.

Results and Discussion

Microstructural Characterization

Morphologies of PbS-PVA nanocomposites and Au-doped PbS-PVA nanocomposites were observed by high-resolution transmission electron microscopy (HRTEM). Figure 1a shows the plane view TEM micrographs of PbS nanoparticles (NPs) synthesized in PVA matrix. The TEM micrograph revealed the formation of PbS NPs embedded in PVA matrix showing PbS NPs with average size of ~7.5 nm. The PbS nanoparticles are quasi-spherical in shape and are well dispersed in the PVA matrix with minimal aggregation. The number of particles per unit area is found to be 6×10^3 m^{-2}. The selected area electron diffraction (SAED) pattern (inset of Fig. 1a) clearly shows the polycrystalline nature of PbS NPs from the formation of circular rings, and the prominent diffraction patterns in the micrograph are indexed as (200), (220) and (311) planes of face centred cubic (fcc) rock salt PbS crystal structure. Figure 1b represents typical HRTEM micrograph of Au-doped PbS in PVA matrix with average

size of ~ 17 nm. The number of Au-doped PbS inside PVA matrix per unit area is found to be 2×10^6 m^{-2}. The SAED pattern confirms face centered cubic (FCC) Au and rock salt PbS phases of the Au-doped PbS-PVA nanocomposites (the top right inset of Fig. 1b. The SAED pattern depicts (200), (220) and (311) diffraction rings with the inter-planar spacing (d_{hkl}) of 0.29 nm, 0.20 nm and 0.17 nm, respectively, of rock salt Au/PbS crystal structure (JCPDS File Card 05-0592).[23] The SAED also shows a ring with index (111), which is due to the contribution from the cubic Au phase which gives rise to a diffraction peak in the x-ray diffraction (XRD) pattern. High-resolution transmission electron microscopy (HRTEM) image (the bottom right inset of Fig. 1b) reveals that Au/PbS NPs have a high-crystalline structure with an inter-planar spacing in the lattice fringes of 0.235 nm (JCPDS File Card 04-0784),[24] indicating the formation of Au nanoclusters oriented in the (111) plane of the fcc lattice. The density of the nanoparticles increases with inclusion of Au NPs which increases polarization leading to a high current ratio of resistive switching memory. Energy-dispersive x-rays (EDX) spectroscopy analysis measurement was employed to investigate the chemical composition of PbS-PVA nanocomposites and Au/PbS-PVA nanocomposites. The EDX spectrum of Au/PbS-PVA nanocomposites is shown in Fig. 1c. The EDX spectrum confirms the presence of lead (Pb), sulphur (S), and gold (Au) in Au/PbS-PVA nanocomposites. The elemental percentage of lead (Pb), sulphur (S), and gold (Au) is depicted in the inset of Fig. 1c. The additional elements C and O arise from carbon-coated copper grids and PVA polymer. Figure 1d shows the cross-sectional SEM image of Al/Au-PbS-PVA nanocomposites/ITO-coated on flexible PET substrate. The FESEM micrograph clearly indicates the ITO bottom electrode, Au-PbS-PVA nanocomposites and Al top electrode with sharp interfaces. The thicknesses of the ITO bottom electrode, Au-PbS-PVA nanocomposite active layer, and Al top electrode are estimated to be 150 nm, 380 nm, and 110 nm, respectively. Figure 1e and f shows the particle size distribution histogram of PbS-PVA nanocomposites and Au/PbS-PVA nanocomposites. The average particle size of PbS-PVA nanocomposites and Au/PbS-PVA nanocomposites is found to be ~ 7.5 nm and ~ 17 nm, respectively. The surface topography of PbS-PVA nanocomposite and Au/PbS-PVA nanocomposite films deposited on ITO-coated flexible PET substrates was studied by atomic force microscopy (AFM) in tapping mode. Figure 2a and b shows the plane view of surface morphology of PbS-PVA nanocomposite and Au/PbS-PVA nanocomposite films, respectively. The surface roughness of PbS-PVA nanocomposite and Au/PbS-PVA nanocomposite films was estimated from AFM topography with a 200 nm × 200 nm scan area. The calculated RMS roughness of PbS-PVA nanocomposites and Au/PbS-PVA nanocomposites is reported to be ~ 39 nm and
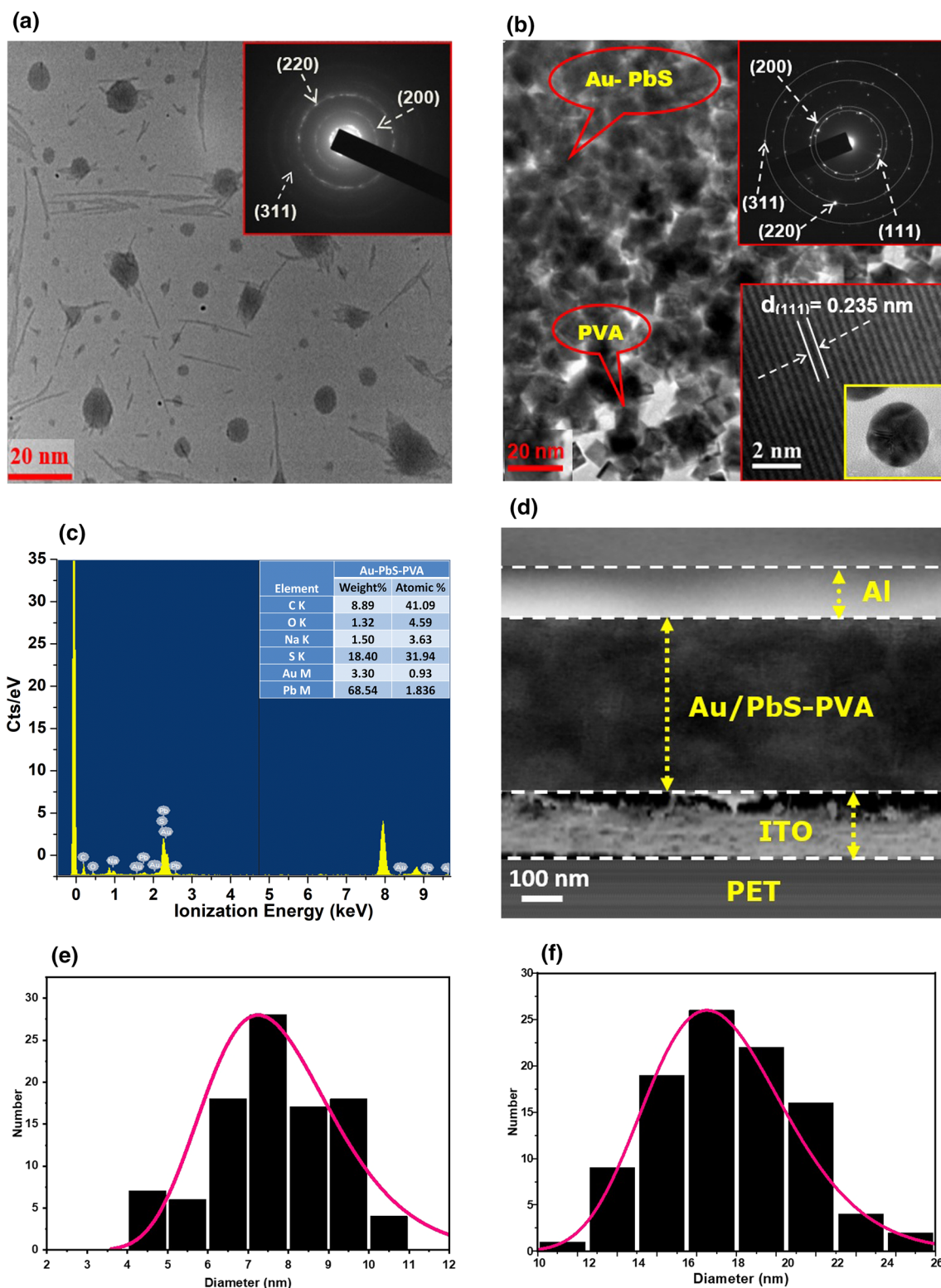
Fig. 1 (a) Plane view TEM micrographs of PbS nanoparticles synthesized in PVA matrix. Selected area electron diffraction pattern (SAED) of PbS nanoparticles (NPs) embedded in PVA matrix (inset). (b) Typical TEM micrograph of Au NPs decorated PbS in PVA matrix. Selected area electron diffraction pattern (SAED) of Au/PbS-PVA nanocomposites (top right inset). HRTEM image showing the Au/PbS-PVA nanocomposites lattice fringes (bottom right inset). (c) Energy dispersive x-ray (EDX) spectra of Au/PbS-PVA nanocomposites (Elemental percentage in the inset). (d) The cross-sectional SEM image of Al/Au-PbS-PVA/ ITO coated flexible PET substrate. (e) Particle size distribution for PbS in PVA matrix. (f) Au/PbS-PVA nanocomposites

~ 67 nm, respectively. The surface roughness of Au-PbS/ PVA films shows higher value due to the presence of Au NPs in PbS-PVA nanocomposite. X-ray diffraction (XRD) measurements were carried out to identify the crystal structure of lead sulfide (PbS) embedded in PVA matrix and

reveal the presence of Au NPs embedded in the PbS-PVA nanocomposite sample. The XRD spectra of undoped PbS-PVA nanocomposites and Au-doped PbS/PVA nanocomposites deposited on ITO-coated glass substrates are shown in Fig. 3a. The XRD result shows that undoped PbS-PVA

Fig. 2 (a) Plane view of AFM surface topography of a PbS-PVA nanocomposite films and (b) Au/PbS-PVA nanocomposite films deposited on flexible ITO coated PET substrates
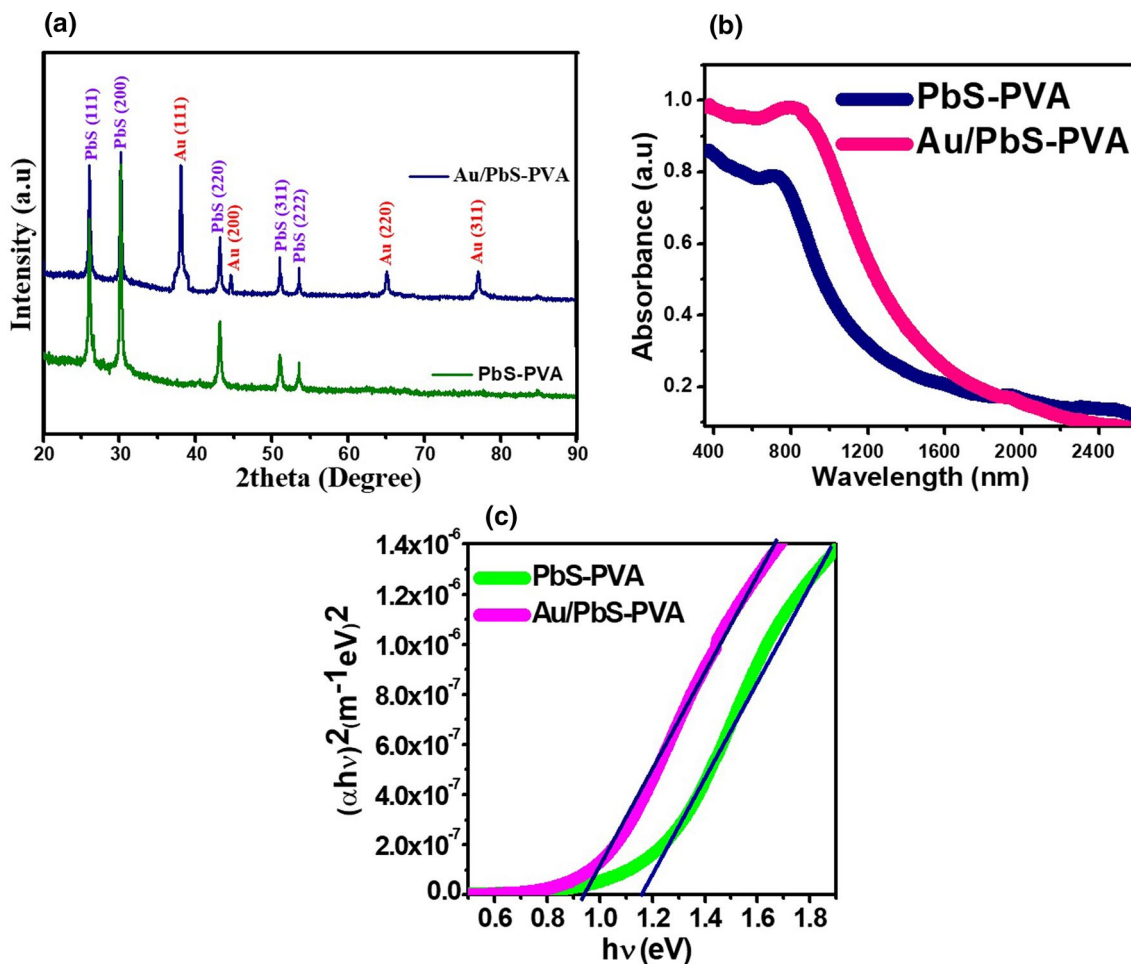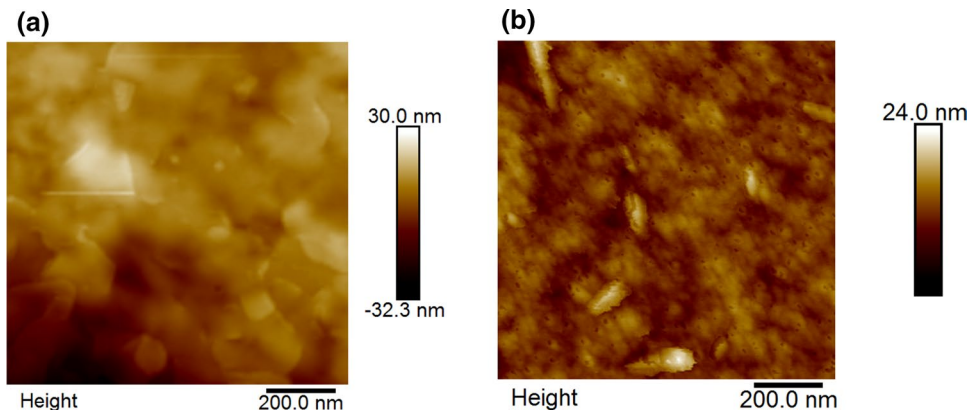
Fig. 3 (a) X-ray (Cu-Kα radiation) diffraction patterns of undoped PbS-PVA nanocomposites and Au-doped PbS-PVA nanocomposites deposited on ITO coated glass substrates. (b) UV-visible absorption spectra of undoped PbS-PVA nanocomposites and Au-doped PbS-PVA nanocomposites. (c) $(\alpha h\nu)^2$ vs $h\nu$ plot for determining the band gap

nanocomposites and Au-doped PbS-PVA nanocomposites are highly crystalline. For PbS-PVA nanocomposites sample, the dominant peaks at 2θ values of 26.09°, 30.18°, 43.08°,51.04° and 53.55° which are assigned to (111), (200), (220), (311) and (222) planes of PbS with lattice parameters a = b = c = 5.931 Å (JCPDS File Card 78-1901) indicating the fcc rock salt structure.[25] The XRD spectra of Au/PbS-PVA depicts four additional peaks at 38.1°, 44.3°, 64.5° and 77.7° as assigned to (111), (200), (220), (311) associated with fcc structure of gold. The intense diffraction at angle 38.1° is due to preferred growth orientation of gold along (111) direction. XRD peaks of PbS do not show any shift and broadening which indicates that crystal structure of PbS remains unaltered with the inclusion of gold nanoparticles. The XRD results are in consistent with HRTEM results.

Optical Properties

For the purpose of investigating the influence of Au doping on the optical absorption of PbS-PVA nanocomposites, ultraviolet (UV)-visible absorption spectroscopy was used to study the change of absorption. Figure 3b shows the absorption spectra of undoped PbS-PVA nanocomposites and Au-doped PbS-PVA nanocomposites deposited on flexible PET substrates. The broad absorption peak in the wavelength range of 400–2600 nm can be attributed to the intrinsic band gap of PbS nanoparticles (~1.15 eV), which is generally related to electronic transition from the valance band to conduction band.[26] It is clearly seen that the presence of Au ions made the absorption band edge shift toward higher wavelength, namely a redshift, which means the Au-doped PbS-PVA nanocomposite possessed a narrower band gap that is good for a redshift of light adsorption and increases electrical conductivity.[25] The optical band gaps (E_g) of the prepared samples have been calculated from UV-Vis spectroscopy by using the following Tauc's formula[27]:

$$(\alpha h \nu)^{\frac{1}{n}} = A\left(h\nu - E_g\right) \tag{1}$$

where α is the absorption coefficient, h is the Planck constant, ν is the frequency and it is the reciprocal of wavelength. A is the absorbance of the sample, E_g is the optical band gap, and the exponent n depends on the type of transition. As PbS is a direct band gap semiconductor, $n = \frac{1}{2}$ for direct allowed transition. The optical band gap values are estimated by extrapolating the linear part of the plot $(\alpha h \nu)^2$ versus $(h\nu)$ on the energy axis $(h\nu)$, as shown in the inset of Fig. 3c. The calculated optical band gap energy for pristine PbS-PVA nanocomposite film and Au-doped PbS-PVA nanocomposite film are found to be 1.15 eV and 0.95 eV, respectively. The narrowing of the optical band gap energy of Au-doped PbS-PVA nanocomposite film indicated an obvious redshift of light adsorption. The reduction of the

optical energy gap is due to intense doping of Au NPs. This may be attributed to the band shrinkage effect because of increasing charge carriers.[28] Figure 4a represents the full-range XPS spectrum of Au-doped PbS-PVA nanocomposites which demonstrates clearly the presence of gold (Au), lead (Pb), sulfur (S), carbon (C) and oxygen (O) in the sample. Figure 4b represents the detailed scan of Au 4f peaks which can be decovulated to two peaks, Au $4f_{5/2}$ and Au $4f_{7/2}$, at binding energies 87.1 eV and 83.4 eV, respectively. The binding energy of 4f electrons in Au is shifted to the lower energy side as compared to the bulk which indicates that the surface charge of Au nanoparticles is partially negative without any chemical bonding with PbS. The HOMO level of PbS is near the Fermi level of Au which may result in transfer of electrons from PbS to gold that may result in an increase in charge density on the surface of Au NPs.[29,30] A detailed scan of S2p spectrum as shown in Fig. 4c can be fitted into four peaks. The two peaks at 162 eV and 163 eV can be attributed to $2p_{3/2}$ and $2p_{1/2}$ of the lower valence state of S^{2-}. The characteristic peak observed around 162 eV may be assigned to sulphide S2p which indicates the formation of PbS fcc structure in accordance with XRD results. The binding energy at 167 eV and 168 eV is from S^{6+} $2p_{1/2}$ and S^{6+} $2p_{3/2}$, respectively, suggesting that S is in the highest oxidation state (+6). These peak positions belong to the strongly oxidised sulphate group. Figure 4d presents the XPS spectra of two deconvulated Pb 4f peaks corresponding to the Pb ($4f_{7/2}$) and Pb ($4f_{5/2}$) core levels of the Pb^{2+} cations associated with PbO formation. They are located at the binding energies of 137 eV and 142 eV, respectively. The energy spacing between two position peaks is 5 eV may reflect binding between Pb and S atoms. In other words, the binding energy peak around 137 eV is typically assigned to Pb-S bonding.[31–33]

Electrical Characterization

The electrical characteristics of the non-volatile memory device were investigated by using current-voltage (I-V) source measurements. The samples fabricated for investigations are (i) Al/PbS-PVA/ITO/flexible PET substrate (denoted as D1), (ii) Al/Au/PbS-PVA/ITO/flexible PET substrate (denoted as D2). For electrical measurements, Al top electrodes (TE) were linked to the negative ('-') terminal of the source meter, and ITO bottom electrodes (BE) were connected to the positive ('+') terminal of the source meter. The schematic diagram of the flexible D2 memory device is shown in Fig. 5a. Figure 5b shows the I-V switching characteristics of the D2 memory device. The external stimulation is provided to the device with voltage sequence of 0V→ +2V→ 0V→ −2V→ 0V. The compliance current is set at 10 mA to prevent permanent dielectric breakdown of the D2 device (Icc). The electrical hysteresis behaviour
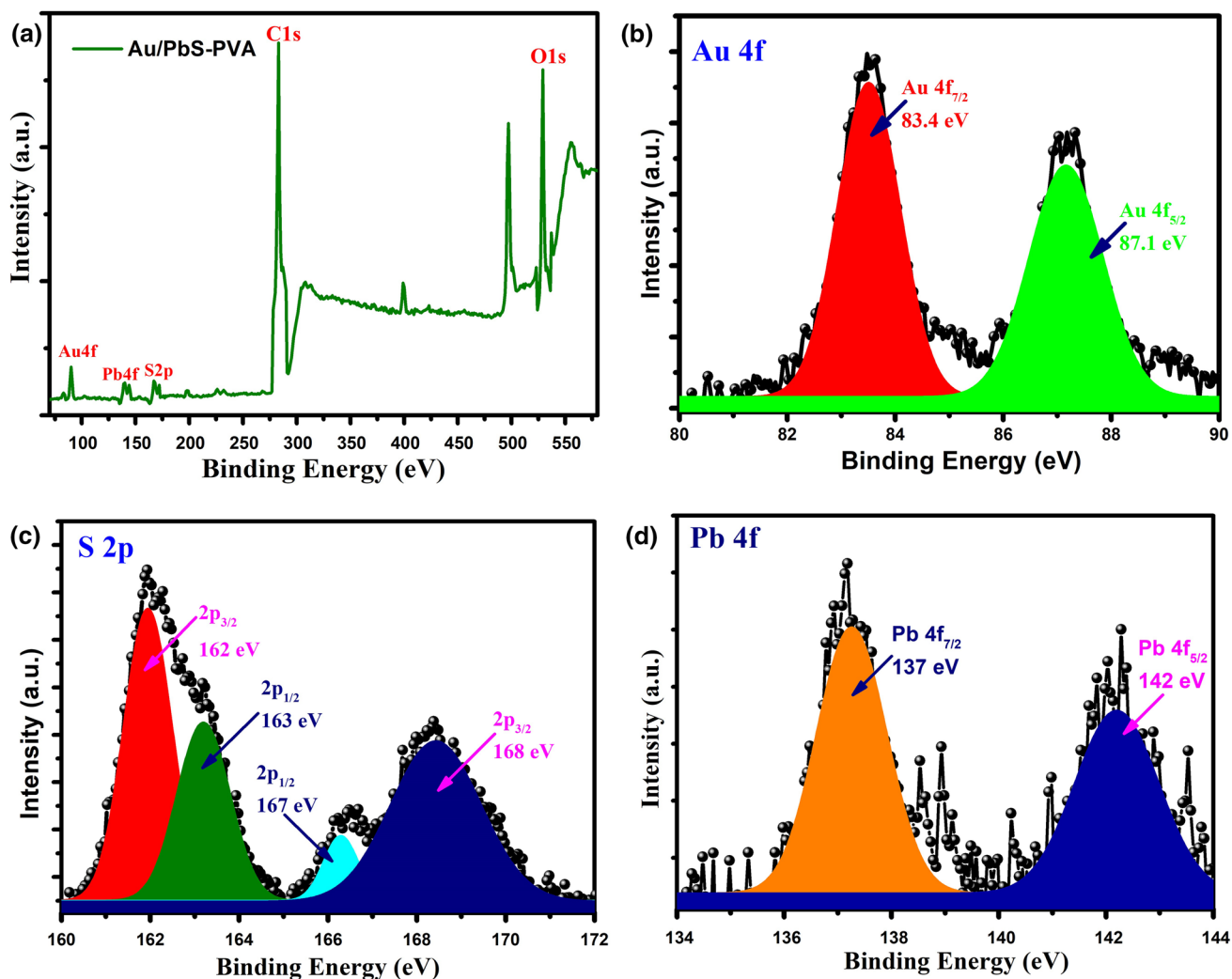
Fig. 4 (a) Typical XPS survey scan spectrum of Au/PbS-PVA nanocomposites. The high resolution XPS spectra of (b) Au 4f peak (c) S 2p peak and (d) Pb 4f peak

is observed in electrical measurements which is essential for resistive switching memory. Initially, the device was in a high-resistance state (HRS) and the device current was 5 nA at a read voltage of 0.2 V. When the device is subjected to forward voltage sweep, the current increases gradually along the sweeping direction and a rapid increase in current from 6.7×10^{-8} A to 2×10^{-2} A is observed at a voltage of $+1$ V, indicating the resistive switching from HRS to a low-resistance state (LRS). This switching process from OFF-state (i.e., HRS) to ON-state (i.e., LRS) is referred to as the 'SET' process, and in other words, termed as the writing process. After reaching LRS, the SET state is maintained from $+2.0$ V to -1.4 V, while reverse sweeping. The device then switches from LRS to HRS at -1.4 V. This transition from LRS to HRS is referred to as the 'RESET' process. In other words, this process is known as erasing. The SET voltage and RESET voltage occurs at $+1$ V and

-1.4 V, respectively. The existence of two resistance states, namely, high resistance state (i.e., OFF state) and low resistance state (i.e., ON state) was maintained even after removal of the applied bias voltage, exhibiting bistable non-volatile memory behaviour of the D2 device. The reversible resistance switching between HRS and LRS was repeated for 100 cycles and the two resistance states showed stability. The current ratio (I_{ON}/I_{OFF}) between the ON- and OFF states is about 10^6 in magnitude at a reading voltage of 0.5 V as shown in Fig. 5b. The high value of current switching ratio confirms the presence of multilevel cells for storage that contribute to high current density memory device. Thus, the device has potential for application in flexible memory devices.[34,35]

In order to understand the effect of gold nanoparticles on the D2 memory device, a control sample, device D1, has been fabricated and corresponding current-voltage
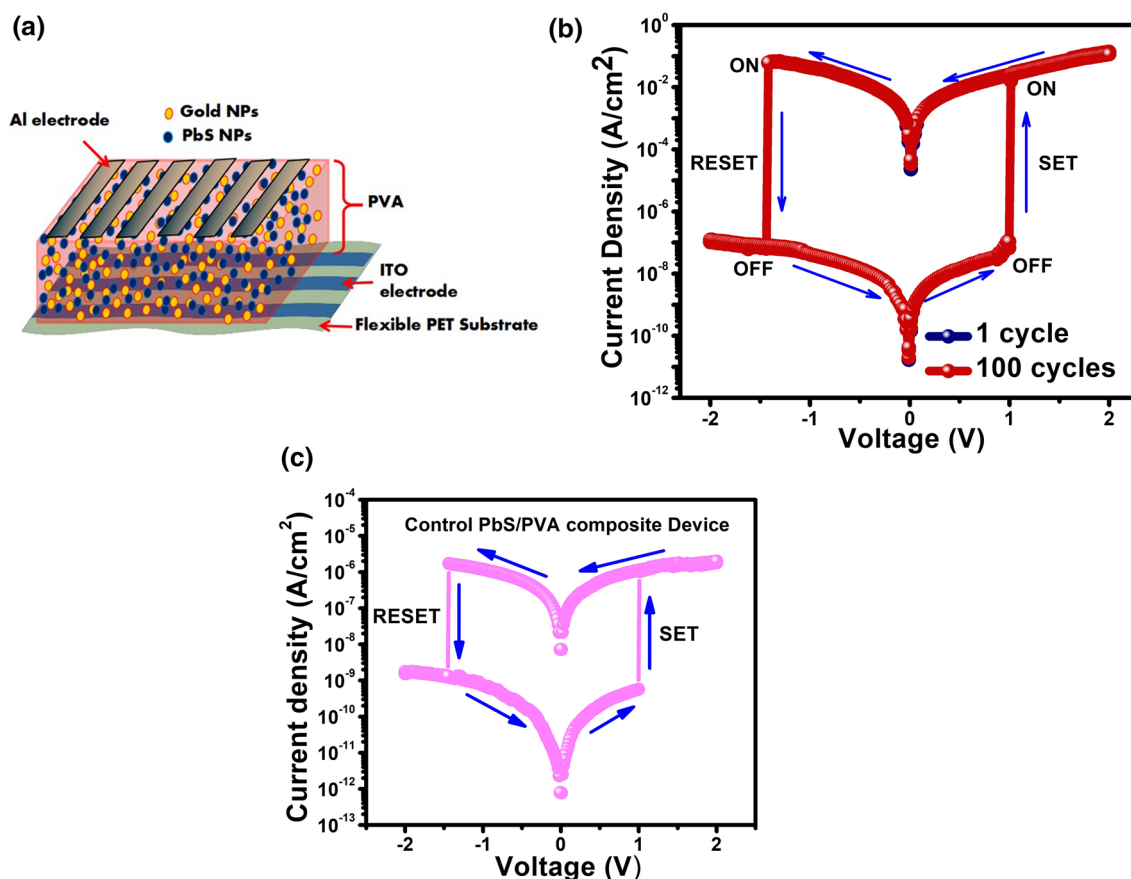
Fig. 5 (a) Schematic diagram of Al/Au-PbS-PVA/ITO coated flexible PET substrate device. I-V switching characteristics of the (b) Al/Au-PbS-PVA/ITO coated flexible PET substrate device and (c) Al/PbS-PVA/ITO coated flexible PET substrate

characteristics were measured for comparison as shown in Fig. 5c. Applying the positive bias to device D1, the current started increasing gradually and at a voltage of 1V the resistance changes from HRS (i.e., OFF state) to LRS (i.e., ON state). This ON state is maintained from 2 V to − 2 V during reverse sweeping. Further, the current decreases suddenly at a voltage of − 1.45 V. The current ratio (I_{ON}/I_{OFF}) for device D1 is 10^3. The performance of device D1 was inferior as compared to the D2 memory device. The higher ON/OFF current ratio up to 10^6 achieved for device D2 is due to inclusion of gold nanoparticles in the PbS-PVA matrix. The enhancement in resistive switching behaviour may be attributed to the increased of charge injection that further improves storage properties of PbS nanoparticles inside the polymer PVA matrix.[36]

Conduction Mechanism

By fitting the I-V characteristics in a log-log scale, the conduction mechanism of the D2 memory device was explored in depth. Figure 6a and b shows linear fitting of I-V characteristics in the SET and RESET process, respectively. In the low-voltage region of the SET process, the I-V characteristic exhibits ohmic conduction ($I \propto V$) with a slope of ~1 attributed to the thermally generated electrons. As the voltage increases, the conduction follows Child's square law ($I \propto V^2$) with a slope of ~2.5 that indicates domination of injected charge carriers over thermionic emission, where the current is fully controlled by shallow traps with space charge formed by sulphur ions. Thereafter, the trap becomes saturated with sufficient injection of charges. These injected carriers can move freely, and consequently, an abrupt increase in current results in the switching of device D2 from HRS to LRS. The I-V characteristics in LRS follows ohmic conduction with a slope of ~ 1.1 which confirms the formation of highly conductive filaments in the composite layer. Figure 6b represents I-V characteristics in the RESET process that follows similar conduction behaviour. The conduction follows a trap unfilled space-charge limited current (SCLC) model with a slope of ~ 2.4 in which all the injected charge carriers come out of traps leading to rupture of filaments. As a result, the device switches from LRS to HRS. Figure 6c is a linearly fitted plot of ln (I/V) versus $V^{1/2}$ which corresponds to the Poole-Frenkel (PF) emission model for the
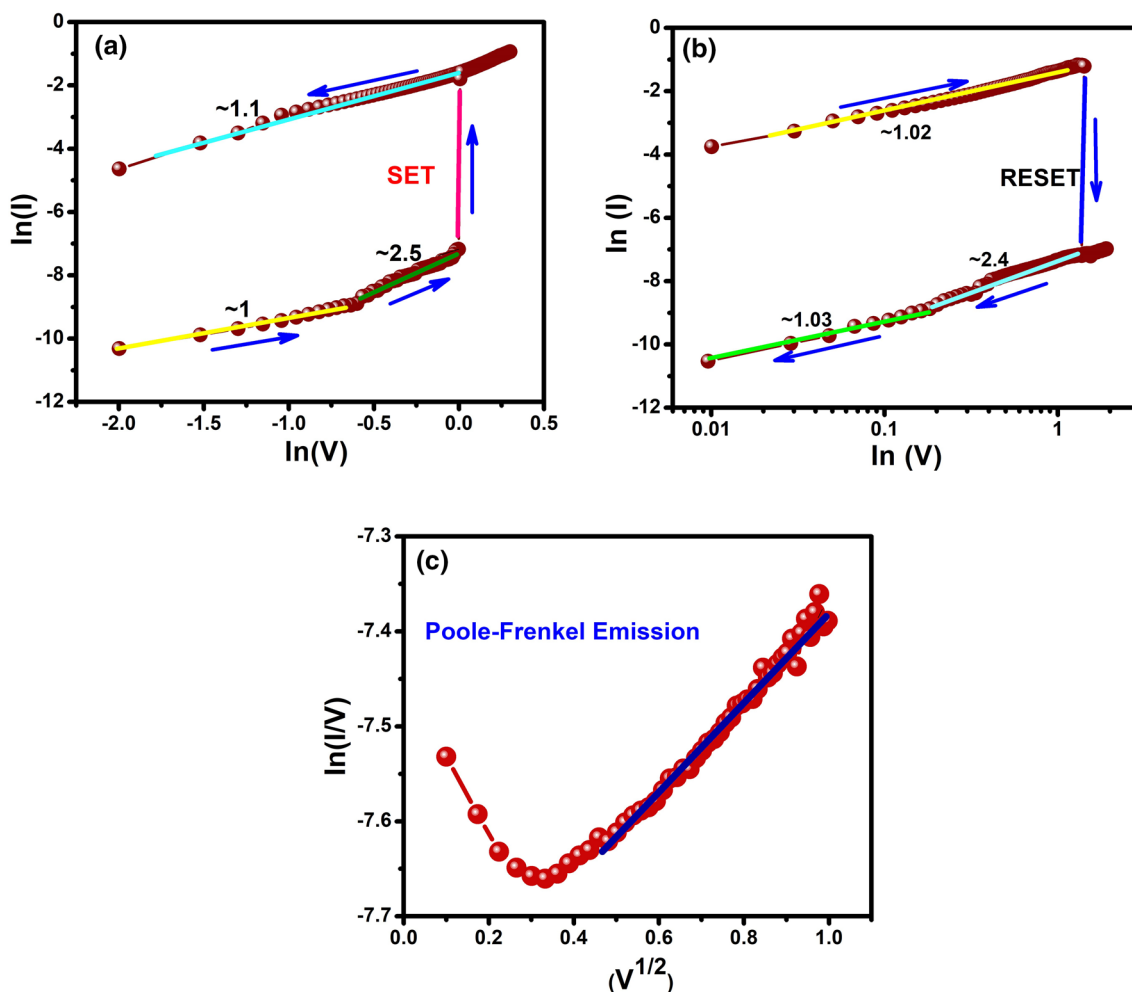
Fig. 6 (a) Linear fitting for the I-V curve of the D2 memory device on a log-log scale a SET process, (b) RESET process and (c) shows the Poole-Frenkel emission fit

D2 memory device. It is observed that the plot of ln (I/V) against $V^{1/2}$ is not linear which means the conduction in this D2 device is fully controlled by space charges formed by sulfur ions owing to the SCLC mechanism.

In the D1 device, when voltage is applied lead cations and sulfur anions are induced to form space charges. These charges are trapped by defects resulting in expedition of polarization of space charge. As a result, the charge carrier reaches the bottom electrodes constructing the current pathways known as filament formation between the top and bottom electrodes. Thus, the D1 device shows resistive switching behavior with the current ratio (I_{ON}/I_{OFF}) of 10^{-3}. It is noted that Au NPs play an important role in resistive switching behaviour of the D2 memory device. The switching current ratio (I_{ON}/I_{OFF}) in the D2 memory device increases by 10^6 with the inclusion of Au NPs. Hence, the switching current ratio of the D2 memory device is higher than the control D1device.The rise in switching current ratio

of the D2 memory device may be attributed to charge injection properties of Au NPs. Further, the charged state of Au NPs may extend to space charge field that may inhibit or speed up carrier transport.[37] The trapped charge carriers can remain inside the Au NPs for comparably elongated time even after the removal of applied bias.[38]

The SCLC transport mechanism for the D2 device is due to the charge trapping states available in the PbS NPs as well as Au NPs acting as trap centers. The origin of resistive switching behaviour may be attributed to the formation and rupture of conductive filaments between top and bottom electrodes. This is due to current pathways formed by lead (Pb) vacancies in the active region. Figure 7a shows schematic diagrams of energy levels corresponding to the D2 memory device's operating mechanism. The reported values of work function for Al, Au, PbS and ITO have been utilized in the proposed model while the electron affinity of the PVA barrier is assumed to be 1.5 eV, similar to that of

a non-conducting polymer. Initially, when positive voltage is applied to the top electrode of the D2 memory device, the oxidation of PbS takes place results in formation of positively charged Pb^{2+} ions (holes) and negatively charged S^{2-} ions (electrons) as depicted in Fig. 7b. With the further increase of voltage as shown in Fig. 7c, Pb^{2+} vacancies start migrating toward the bottom electrode and S^{2-} ions move towards the top electrode. Since Au NPs are negatively charged, they accumulate near the Al top electrode. Au NPs can access the electrons causing them to be trapped inside acting as trap centers because of the high potential barrier between the electron affinity of PbS and the work function of Au NPs. As a result, S^{2-} ions moving towards the top electrode encounter these traps and become trapped in these sites causing generation of an internal electric field. The high electric field and trapped electrons result in separation

of charges which creates various dipoles and enhances the polarization effect in the switching layer. With the inclusion of Au NPs, the polarization effect multiplies in the device. Because of this effect, the density of lead ions increase and results in their acceleration towards the bottom electrode. When applied positive voltage reaches the SET voltage, i.e. 1 V, a highly conductive path is formed between top and bottom electrodes which results in resistive switching of the D2 device from HRS to LRS known as the SET process. Conversely, when the negative voltage is applied to the top Al electrode, negatively charged Au NPs are repelled by the Al electrode. The S^{2-} ions (electrons) come out of traps and move towards the bottom electrodes and Pb^{2+} vacancies (holes) move toward the top Al electrode resulting in rupture of the conductive filament, which is known as the RESET state, as shown in Fig. 7d. Figure 8a represents the
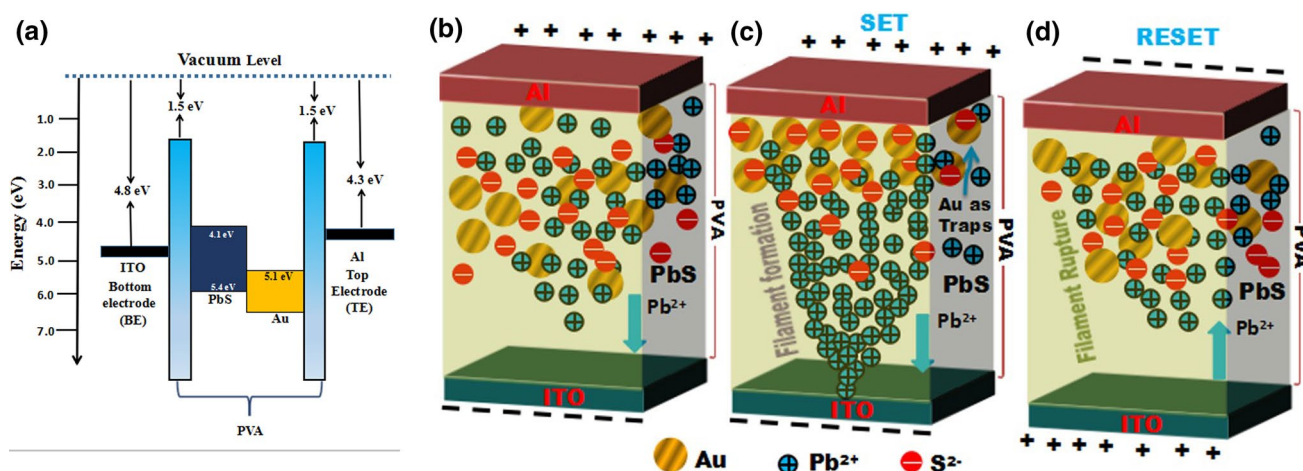
Fig. 7 (a) Schematic diagrams of energy level corresponding to the operating mechanism of D2 device. Schematic diagrams of the electronic structures corresponding to the operating mechanisms for D2 device at the (b) low voltage (c) SET voltage and the (d) RESET voltage
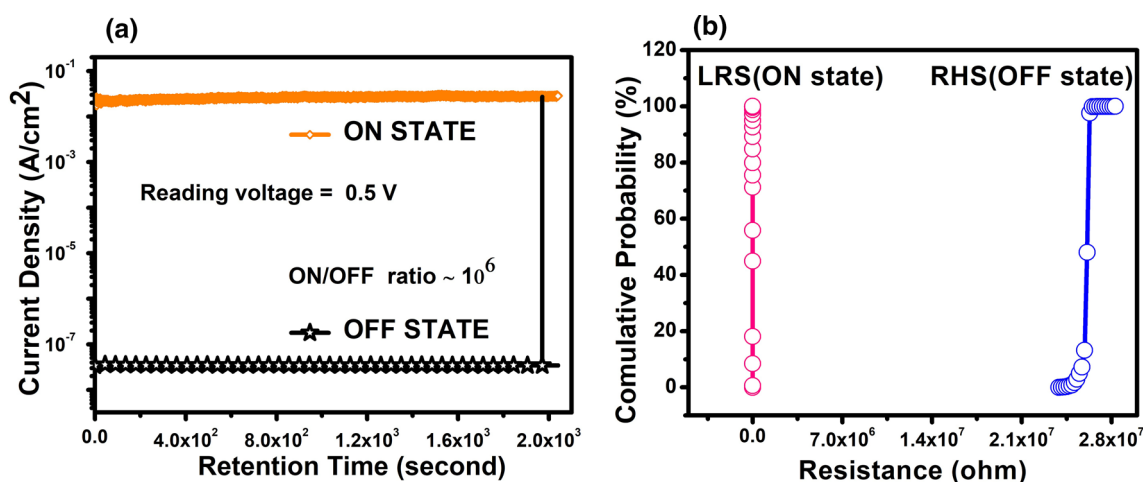

Fig. 8 (a) Retention time measurement of the D2 device with a read voltage of 0.5 V on logarithmic scale. (b) Cumulative probability of D2 memory device

data retention characteristics of the ON-state and OFF-state currents varying as functions of time for the D2 memory devices with a read voltage of 0.5 V at room temperature on a logarithmic scale. No discernible degradation of the D2 memory device was observed in either the ON state or OFF state for 2×10^3 -s continuous operation, which shows excellent stability of the device, maintaining a high current ratio (I_{ON}/I_{OFF}) of about ~10^6 . Both the ON and OFF states have current density values of 2.8×10^{-2}A and 3.4×10^{-8}A, respectively. These observations show that the D2 memory device possesses outstanding stability and reproducibility, making it ideal for non-volatile memory applications. Moreover, the cumulative probability of the D2 memory device was examined in both ON states and OFF states. Figure 8b depicts the cumulative probability of resistance switching of the D2 memory device. The resistance values measured at a read voltage of 0.5 V were plotted as LRS and HRS. The distribution of LRS was quite narrow compared to the distribution of HRS. The average values of LRS and HRS were found to be 3.4 Ω and 3 MΩ, respectively, with a high

resistance ratio (LRS/HRS) as ~10^6 between the two resistance states. The D2 memory device proposed here is a promising candidate for high-performance flexible non-volatile memory devices.

Flexibility Study

The D2 memory device has been shown to be a good choice for non-volatile bistable memory in flexible electronic applications. Figure 9a–d shows the I-V switching characteristics of a non-volatile bistable memory device at 180° (without bending) and with bending angle 70°, 90° and 120° of the PET substrates, respectively. The pictorial images for individual cases have been represented in the respective insets. Even after bending the device from 180° to 70° angles, I-V switching characteristics remained consistent which meets the condition for desirable flexible electronic applications.
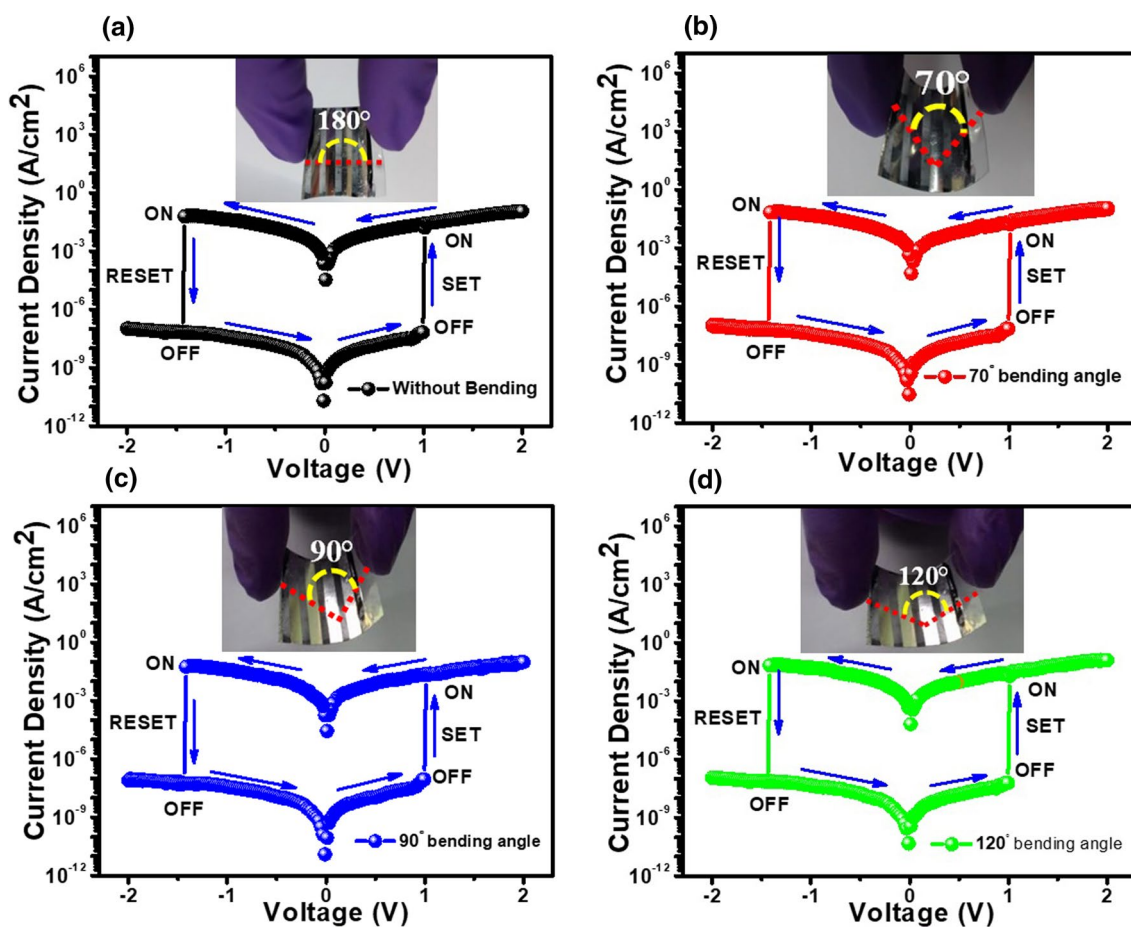
Fig. 9 (a) I-V resistive switching characteristic of the D2 memory device at 180° (without bending), (b) I-V switching characteristic were recorded at 70° bending angle, (c) I-V switching characteristic were recorded at 90° bending angle and (d) I-V switching characteristic were recorded at 120° bending angles of the PET substrates with corresponding pictorial image represented in the inset

Conclusion

In summary, we have demonstrated the flexible non-volatile memory device using Au/PbS-PVA nanocomposites deposited on ITO coated flexible PET substrate. TEM micrograph revealed the formation of Au/PbS nanoparticles in the PVA matrix. The SAED pattern confirms fcc Au and rock salt PbS phases of the Au-doped PbS-PVA nanocomposites. The EDX spectrum of nanocomposites clearly indicates the presence of Au, Pb and S in Au/PbS-PVA nanocomposites. AFM topography of 1 µm × 1 µm scan area was used to investigate the surface roughness of PbS-PVA nancomposites and Au/PbS-PVA nanocomposite film. The PbS-PVA nanocomposites and Au/PbS-PVA nanocomposites were reported to have surface roughness of 46 nm and 78 nm, respectively. The XRD result shows that undoped PbS-PVA nanocomposites and Au-doped PbS-PVA nanocomposites are highly crystalline. The UV results revealed the narrowing of the optical band gap energy when Au nanoparticles were doped to PbS-PVA nanocomposites, indicating an obvious redshift of light adsorption. This may be attributed to the band shrinkage effect because of increasing charge carriers. The XPS survey scan of nanocomposites depicts the presence of oxidation states of Pb, S and Au ions. The charge transport mechanism may be accredited to SCLC by intently analyzing I-V characteristics of the prepared nanocomposites. The retention time measurement of device emphasizes its stability traits. The fabricated D2 memory device showed stable nature by passing endurance test against 100 cycles. The D2 memory device was measured for retention, stability and flexibility by constantly bending D2 device from 70° bending angle to 120° bending angle and without bending (180°). Interestingly, the resistances of both ON state and OFF state unveiled no degradation in the memory device. Moreover, I-V characteristics parameters after bending the D2 device at 70°, 90°, 120° and 180° (without bending) angles remained stable and unvariable. Therefore, the fabricated D2 memory device has high potential to be used in advanced flexible non-volatile memory application due to its stable and mechanical flexible properties.

Data Availability The data that support the findings of this study are available from the corresponding author upon reasonable request.

Declarations

Conflict of interest There is no conflict to declare.

References

1. E.W. Lim, and R. Ismail, Conduction Mechanism of Valence Change Resistive Switching Memory: A Survey. *Electronics* 4, 586 (2015). https://doi.org/10.3390/electronics4030586.
2. F. Mitri, A. De Iacovo, M. De Luca, A. Pecora, and L. Colace, Lead Sulphide Colloidal Quantum Dots for Room Temperature NO 2 gas Sensors. *Sci. Rep.* 10, 1 (2020). https://doi.org/10.1038/s41598-020-69478-x.
3. S.S. Godara, and P.K. Mahato, Potential Applications of Hybrid Nanocomposites. *Mater. Today: Proc.* 18, 5327 (2019). https://doi.org/10.1016/j.matpr.2019.07.557.
4. A. Pirashanthan, D. Velauthapillai, N. Robertson, and P. Rajarajan, Lithium Doped Poly (3-Hexylthiophene) for Efficient Hole Transporter and Sensitizer in Metal free Quaterthiophene dye Treated Hybrid Solar Cells. *Sci. Rep.* 11, 1 (2021). https://doi.org/10.1038/s41598-021-99762-3.
5. M. Gu, Q. Zhang, and S. Lamon, Nanomaterials for Optical Data Storage. *Nat. Rev. Mater.* 1, 1 (2016). https://doi.org/10.1038/natrevmats.2016.70.
6. T.W. Kim, Y. Yang, F. Li, and W.L. Kwan, Electrical Memory Devices Based on Inorganic/Organic Nanocomposites. *NPG Asia Mater.* 4, e18 (2012). https://doi.org/10.1038/am.2012.32.
7. C.D. Schuman, S.R. Kulkarni, M. Parsa, J.P. Mitchell, P. Date, and B. Kay, Opportunities for Neuromorphic Computing Algorithms and Applications. *Nat. Comput. Sci.* (2022). https://doi.org/10.1038/s43588-021-00184-y.
8. J.J. Yang, D.B. Strukov, and D.R. Stewart, Memristive devices for computing. *Nat. Nanotechnol.* 8, 13 (2013). https://doi.org/10.1038/nnano.2012.240.
9. I. Boybat, M.L. Gallo, S.R. Nandakumar, T. Moraitis, T. Parnell, T. Tuma, B. Rajendran, Y. Leblebici, A. Sebastian, and E. Eleftheriou, Neuromorphic computing with Multi-memristive synapses. *Nat. Commun.* 9, 2514 (2018). https://doi.org/10.1038/s41467-018-04933-y.
10. J. Zheng, B. Cheng, F. Wu, X. Su, Y. Xiao, R. Guo, and S. Lei, Modulation of Surface Trap Induced Resistive Switching by Electrode Annealing in Individual PbS Micro/Nanowire-Based Devices for Resistance Random Access Memory. *ACS Appl. Mater. Interfaces* 6, 20812 (2014). https://doi.org/10.1021/am505101w.
11. X. Yan, Y. Pei, H. Chen, J. Zhao, Z. Zhou, H. Wang, and P. Zhou, Self-Assembled networked PbS Distribution Quantum dots for Resistive Switching and Artificial Synapse Performance Boost of Memristors. *Adv. Mater.* 31, 1805284 (2019). https://doi.org/10.1002/adma.201805284.
12. J.C. Scott, and L.D. Bozano, Nonvolatile Memory Elements Based on Organic Materials. *Adv. Mater.* 19, 1452 (2007). https://doi.org/10.1002/adma.200602564.
13. J.J.L. Hmar, T. Majumder, and S.P. Mondal, Growth and Characterisics of PbS/Polyvinyl Alcohol Nanocomposites for Flexible High Dielectric Thin Film Applications. *Thin Solid Films* 598, 243 (2016). https://doi.org/10.1016/j.tsf.2015.12.032.
14. S. Sarma, and P. Datta, Characteristics of Poly (Vinyl Alcohol)/ Lead Sulphide Quantum Dot Device. *Nanosci. Nanotechnol. Lett.* 2, 261 (2010). https://doi.org/10.1166/nnl.2010.1091.
15. Z. Chen, Y. Yu, L. Jin, Y. Li, Q. Li, T. Li, and J. Yao, Broadband Photoelectric Tunable Quantum Dot Based Resistive Random Access Memory. *J. Mater. Chem. C* 8, 2178 (2020). https://doi.org/10.1039/C9TC06230K.
16. N. Zhang, C. Han, X. Fu, and Y.J. Xu, Function-Oriented Engineering of Metal-Based Nanohybrids for Photoredox Catalysis: Exerting Plasmonic Effect and Beyond. *Chem* 4, 1832 (2018). https://doi.org/10.1016/j.chempr.2018.05.005.

17. K. Tanabe, Field Enhancement Around Metal Nanoparticles and nanoshells: A Systematic Investigation. *J. Phys. Chem. C* 112, 15721 (2008). https://doi.org/10.1021/jp8060009.

18. Y. Li, Q. Qian, X. Zhu, Y. Li, M. Zhang, J. Li, and Q. Zhang, Recent Advances in Organic-Based Materials for Resistive Memory Applications. *InfoMat* 2, 995 (2020). https://doi.org/10.1002/inf2.12120.

19. H. Yu, Y. Peng, Y. Yang, and Z.Y. Li, Plasmon-Enhanced Light–Matter Interactions and Applications. *NpjComput. Mater.* 5, 1 (2019). https://doi.org/10.1038/s41524-019-0184-1.

20. I. Venditti, Gold Nanoparticles in Photonic Crystals Applications: A Review. *Materials* 10, 97 (2017). https://doi.org/10.3390/ma10020097.

21. Y. Zhou, S.T. Han, P. Sonar, and V.A.L. Roy, Nonvolatile Multilevel Data Storage Memory Device from Controlled Ambipolar Charge Trapping Mechanism. *Sci. Rep.* 3, 1 (2013). https://doi.org/10.1038/srep02319.

22. N. Gogurla, S.P. Mondal, A.K. Sinha, A.K. Katiyar, W. Banerjee, S.C. Kundu, and S.K. Ray, Transparent and Flexible Resistive Switching Memory Devices with a Very High ON/OFF Ratio Using Gold Nanoparticles Embedded in a Silk Protein Matrix. *Nanotechnology* 24, 345202 (2013). https://doi.org/10.1088/0957-4484/24/34/345202.

23. H. Hosokawa, R. Tamaki, T. Sawada, A. Okonogi, H. Sato, Y. Ogomi, and T. Yano, Solution-Processed Intermediate-Band Solar Cells with Lead Sulfide Quantum Dots and Lead Halide Perovskites. *Nat. Commun.* 10, 1 (2019). https://doi.org/10.1038/s41467-018-07655-3.

24. N. Gogurla, A.K. Sinha, D. Naskar, S.C. Kundu, and S.K. Ray, Metal Nanoparticles Triggered Persistent Negative Photoconductivity in silk Protein Hydrogels. *Nanoscale* 8, 7695 (2016). https://doi.org/10.1039/C6NR01494A.

25. H. Zhao, M. Chaker, and D. Ma, Self-Selective Recovery of Photoluminescence in Amphiphilic Polymer Encapsulated PbS Quantum Dots. *Phys. Chem. Chem. Phys.* 12, 14754 (2010). https://doi.org/10.1039/C0CP01305F.

26. P.T. Bailey, M.W. O'brien, and S. Rabii, Direct-Transition Optical Absorption in PbS, PbSe, and PbTe from Relativistic Augmented-Plane-Wave Functions. *Phys. Rev. Lett.* 179, 735 (1969). https://doi.org/10.1103/PhysRev.179.735.

27. S. Thangavel, S. Ganesan, S. Chandramohan, P. Sudhagar, Y.S. Kang, and C.H. Hong, Band Gap Engineering in PbS Nanostructured Thin Films From Near-Infrared Down to Visible Range by in Situ Cd-Doping. *J. Alloys Compd.* 495, 234 (2010). https://doi.org/10.1016/j.jallcom.2010.01.135.

28. J. Yang, H.I. Elim, Q. Zhang, J.Y. Lee, and W. Ji, Rational Synthesis, Self-assembly, and Optical Properties of PbS−Au Heterogeneous Nanostructures via Preferential Deposition. *J. Am. Chem. Soc.* 128, 11921 (2006). https://doi.org/10.1021/ja062494r.

29. K.F. Berggren, and B.E. Sernelius, Band-Gap Narrowing in Heavily Doped Many-Valley Semiconductors. *Phys. Rev. B Condens. Matter* 24, 1971 (1981). https://doi.org/10.1103/PhysRevB.24.1971.

30. J. Koo, J. Yang, B. Cho, H. Jo, K.H. Lee, and M.S. Kang, Nonvolatile Electric Double-Layer Transistor Memory Devices Embedded with Au Nanoparticles. *ACS Appl. Mater. Interfaces* 10, 9563 (2018). https://doi.org/10.1021/acsami.8b01902.

31. P. Cui, S. Seo, J. Lee, L. Wang, E. Lee, M. Min, and H. Lee, Nonvolatile Memory Device Using Gold Nanoparticles Covalently Bound to Reduced Graphene Oxide. *Acs Nano* 5, 6826 (2011). https://doi.org/10.1021/nn2021875.

32. V.V. Burungale, R.S. Devan, S.A. Pawar, N.S. Harale, V.L. Patil, V.K. Rao, and P.S. Patil, Chemically Synthesized PbSnanoparticulate Thin Films for a Rapid NO2 Gas Sensor. *Mater Sci Pol* 34, 204 (2016). https://doi.org/10.1515/msp-2016-0001.

33. N. Gogurla, A.K. Sinha, S. Santra, S. Manna, and S.K. Ray, Multifunctional Au-ZnOplasmonic Nanostructures for Enhanced UV Photodetector and Room Temperature NO Sensing Devices. *Sci. Rep.* 4, 1 (2014). https://doi.org/10.1038/srep06483.

34. Y. Jia, C. Wu, B.W. Lee, C. Liu, S. Kang, T. Lee, and W. Lee, Magnetically separable sulfur-doped SnFe2O4/graphenenanohybrids for effective photocatalyticpurification of wastewater under visible light. *J. Hazard. Mater.* 338, 447–457 (2017). https://doi.org/10.1016/j.jhazmat.2017.05.057.

35. F. Lv, K. Ling, T. Zhong, F. Liu, X. Liang, C. Zhu, and W. Kong, Multilevel Resistive Switching Memory Based on a CH 3 NH 3 PbI 3−x Cl x Film with Potassium Chloride Additives. *Nanoscale Res. Lett.* 15, 1 (2020). https://doi.org/10.1186/s11671-020-03356-3.

36. S. Bhattacharjee, P.K. Sarkar, M. Prajapat, and A. Roy, Electrical Reliability, Multilevel Data Storage and Mechanical Stability of MoS2-PMMA Nanocomposite-Based Non-Volatile Memory Device. *J. Phys. D Appl. Phys.* 50, 265103 (2017). https://doi.org/10.1088/1361-6463/aa71e9.

37. W. Shi, H. Zeng, Y. Sahoo, T.Y. Ohulchanskyy, Y. Ding, Z.L. Wang, and P.N. Prasad, A General Approach to Binary and Ternary Hybrid Nanocrystals. *Nano Lett.* 6, 875 (2006). https://doi.org/10.1021/nl0600833.

38. A. Rani, and D.H. Kim, A Mechanistic Study on Graphene-Based NonvolatileReRam. *J. Mater. Chem. C* 4, 11007 (2016). https://doi.org/10.1039/C6TC03509D.